

## ON THE NATURE OF X-RAY SURFACE BRIGHTNESS FLUCTUATIONS IN M87

P. ARÉVALO<sup>1</sup>, E. CHURAZOV<sup>2,3</sup>, I. ZHURAVLEVA<sup>4,5</sup>, W. R. FORMAN<sup>6</sup>, C. JONES<sup>6</sup>

*Draft version February 9, 2022*

### ABSTRACT

X-ray images of galaxy clusters and gas-rich elliptical galaxies show a wealth of small-scale features which reflect fluctuations in density and/or temperature of the intra-cluster medium. In this paper we study these fluctuations in M87/Virgo, to establish whether sound waves/shocks, bubbles or uplifted cold gas dominate the structure. We exploit the strong dependence of the emissivity on density and temperature in different energy bands to distinguish between these processes. Using simulations we demonstrate that our analysis recovers the leading type of fluctuation even in the presence of projection effects and temperature gradients. We confirm the isobaric nature of cool filaments of gas entrained by buoyantly rising bubbles, extending to 7' to the east and south-west, and the adiabatic nature of the weak shocks at 40'' and 3' from the centre. For features of  $\sim 5 - 10$  kpc, we show that the central  $4' \times 4'$  region is dominated by cool structures in pressure equilibrium with the ambient hotter gas while up to 30% of the variance in this region can be ascribed to adiabatic fluctuations. The remaining part of the central  $14' \times 14'$  region, excluding the arms and shocks described above, is dominated by apparently isothermal fluctuations (bubbles) with a possible admixture (at the level of  $\sim 30\%$ ) of adiabatic (sound waves) and by isobaric structures. Larger features, of about 30 kpc, show a stronger contribution from isobaric fluctuations. The results broadly agree with an AGN feedback model mediated by bubbles of relativistic plasma.

### 1. INTRODUCTION

It is well known that the cores of relaxed clusters are strongly perturbed by the outflows of relativistic plasma from a central supermassive black hole (e.g., Bohringer et al. 1995; Churazov et al. 2000; McNamara et al. 2000; Fabian et al. 2000; David et al. 2001; Nulsen et al. 2002; Bîrzan et al. 2004; Dunn & Fabian 2006), suggesting that the amount of energy supplied by the AGN is sufficient to offset gas cooling losses. In the vicinity of the AGN these outflows inflate “cavities/bubbles” in X-ray-emitting gas, which evolve under the action of a buoyancy force (e.g., Churazov et al. 2001; Reynolds et al. 2005). Among plausible channels which transfer energy from the outflow to the gas two processes received much attention: shocks (e.g., Fabian et al. 2003; Forman et al. 2007; Randall et al. 2011) and purely subsonic interaction of the rising bubbles through the X-ray atmosphere, which uplifts cool gas, drives turbulence and excites gravity waves (e.g. Churazov et al. 2002). When these processes are operating at the same time problems arise in differentiating among them in order to assess their

relative roles. In this paper we present a method to broadly identify the type of process, either adiabatic, isobaric or isothermal, that leads to the largest amplitude fluctuations.

Here we use a simple technique (Churazov et al. in prep., see also Zhuravleva et al. 2015) of combining information contained in X-ray images in different energy bands to determine which process makes the largest contribution to the observed fluctuations of the intracluster medium (ICM) in M87/Virgo. We do this by calculating the cross power spectrum for two *Chandra* images and calculating the correlation coefficient and relative amplitudes of fluctuations in several energy bands, namely 0.5–1 keV, 1–3.5 keV and 3.5–7.5 keV. M87/Virgo is a canonical nearby example of a cool core cluster with prominent substructure (e.g., Bohringer et al. 1995; Forman et al. 2005, 2007; Simionescu et al. 2010; Million et al. 2010). Throughout the paper we adopt a distance to M87 of 16 Mpc, 1' corresponds to 4.65 kpc. Its proximity and relatively low gas temperature makes it an ideal object for study based on *Chandra* X-ray images. In an accompanying paper we also apply this analysis to the Perseus cluster (Zhuravleva et al. in prep).

In Sec. 2 we detail the effect that density fluctuations have on X-ray images in different bands and how this can be exploited to differentiate between isobaric, adiabatic and isothermal processes. In Sec. 3 we introduce the power and cross spectrum measures that will be used to characterize the images and we test these statistics with simulated cluster images in Sec. 4. We proceed in Sec. 5 with real cluster data, using *Chandra* images of M87 to determine the dominant type of fluctuation in different regions of the ICM. We interpret these results in term of the energy budget of the fluctuations in Sec. 6 and summarize our findings in Sec. 7.

<sup>1</sup> Instituto de Física y Astronomía, Facultad de Ciencias, Universidad de Valparaíso, Gran Bretaña N 1111, Playa Ancha, Valparaíso, Chile

<sup>2</sup> Max-Planck-Institut für Astrophysik, Karl-Schwarzschild-Strasse 1, 85741 Garching, Germany

<sup>3</sup> Space Research Institute (IKI), Russian Academy of Sciences, Profsoyuznaya 84/32, 117997 Moscow, Russia

<sup>4</sup> Kavli Institute for Particle Astrophysics and Cosmology, Stanford University, 452 Lomita Mall, Stanford, California 94305-4085, USA

<sup>5</sup> Department of Physics, Stanford University, 382 Via Pueblo Mall, Stanford, California 94305-4060, USA

<sup>6</sup> Harvard-Smithsonian Center for Astrophysics, 60 Garden St., Cambridge, MA 02138

## 2. ENERGY DEPENDENT IMPACT OF FLUCTUATIONS ON X-RAY IMAGES.

Many well known processes can cause fluctuations of the ICM density and temperature, which in turn give rise to perturbed X-ray images. Among them: (i) weak shocks and sound waves, (ii) bubbles of relativistic plasma that make X-ray cavities in the gas, (iii) gas displacement from its equilibrium position by buoyant bubbles and subsonic gas motions<sup>7</sup>. Each of these processes will lead to specific *energy dependent* signatures in the X-ray data. For instance, weak shocks and sound waves cause density fluctuations that are positively correlated with temperature fluctuations, as long as thermal conduction is suppressed. On the other hand, cavities associated with the bubbles of relativistic plasma, may have similar depressions in X-ray images in all bands (if the X-ray emissivity of the plasma inside the cavities is small). Finally, subsonically displaced gas lumps may conserve their entropy (once again, provided that conduction is suppressed) and remain in pressure equilibrium with the ambient gas. To maintain pressure balance, these lumps will show anti-correlated temperature and density fluctuations. Thus, even if the true ICM equation of state is adiabatic with  $\gamma = 5/3$ , the observed correlations of the density and temperature fluctuations may not correspond to the  $\gamma = 5/3$  equation of state. Below we classify different types of fluctuations based on their *apparent* equation of state, based on the relative amplitudes of fluctuations present in X-ray images in different energy bands.

As mentioned above, the three aforementioned processes differ by the temperature changes associated with a given amplitude of the density fluctuation. Our goal is to use the images in different energy bands to determine the type of process which gives rise to the density fluctuations. Assuming that the flux emitted per unit volume is  $F = \rho^2 \Lambda_b(T)$ , where  $\rho$  is the density and  $\Lambda_b(T)$  is the emissivity in band  $b$  as a function of temperature  $T$ , all that remains is to calculate the relation between fluctuations of  $\rho$  and  $T$  for each type of process and the emissivity  $\Lambda_b(T)$  for each energy band.

We estimated  $\Lambda_b(T)$  by folding an *XSpec* APEC model through the response function of Chandra's ACIS-I detector, and calculate the flux in each band as a function of temperature, following the procedure described in Forman et al. (2007). For this study we use two energy bands: 1.0–3.5 keV and 3.5–7.5 keV (“soft” and “hard” bands, respectively). The choice of the reference energy bands is driven by two factors. On the one hand, using a combination of images in very soft and very hard bands maximizes the sensitivity to the temperature variations. On the other hand, we need sufficient numbers of counts in each image to produce meaningful results. In Churazov et al. (in prep) we address this issue and show that the pair we use is close to optimal for the temperature characteristic of M87.

For unperturbed temperature and density  $T_0$  and  $\rho_0$ , the perturbed values are

1.  $T = T_0(\rho/\rho_0)^{-1}$  for an isobaric fluctuation,
2.  $T = T_0(\rho/\rho_0)^{2/3}$  for adiabatic fluctuations and
3.  $T = T_0$  for isothermal fluctuations.

Therefore, the change of the flux  $\delta F_b$  in band  $b$  in response to a change in density

$$\rho = G \times \rho_0 \quad (1)$$

is

$$\frac{\delta F_b}{F_b} = \frac{\rho^2 \Lambda_b(T) - \rho_0^2 \Lambda_b(T_0)}{\rho_0^2 \Lambda_b(T_0)} = \frac{\rho_0^2 G^2 \Lambda_b(T_0 G^\eta)}{\rho_0^2 \Lambda_b(T_0)} - 1 \quad (2)$$

$$= \frac{G^2 \Lambda_b(T_0 G^\eta)}{\Lambda_b(T_0)} - 1 \quad (3)$$

where the exponent  $\eta$  is equal -1, 2/3 and 0 for isobaric, adiabatic and isothermal processes, respectively. In the limit of small density fluctuations  $G = 1 + x$ ,

where  $x \ll 1$ , the above expression reduces to  $\frac{\delta F_b}{F_b} =$

$$\left( 2 + \eta \frac{d \log \Lambda_b}{d \log T} \right) x.$$

In Fig.1 we show the ratio of relative amplitudes  $\frac{\delta F_h}{F_h} / \frac{\delta F_s}{F_s}$  of the fluctuations in the hard and soft band images corresponding to the same fluctuation in density. Adiabatic and isobaric cases are shown in the top and bottom panels, respectively. Isothermal fluctuations have equal amplitudes in all bands, i.e. they produce a ratio equal to 1, irrespective of temperature. The green thick line in each set corresponds to the limit of small amplitude fluctuations. To illustrate the nonlinear effects of large amplitude fluctuations we also show the curves for  $G \equiv \frac{\rho}{\rho_0} = 0.5$  (red, solid line),  $G = 1.5$  (blue, dashed line) and  $G = 2.0$  (black, dot-dashed line). In the temperature range relevant to M87, 1.3–3 keV, the three types of process are clearly distinguishable, producing larger, smaller or equal amplitude fluctuations in the hard band than in the soft band for adiabatic, isobaric and isothermal fluctuations, respectively. Factor of  $\sim 2$  fluctuations in density shows substantial deviations from the small amplitude limit and marked asymmetry between positive and negative fluctuations ( $G = 2$  or  $G = 0.5$ ). For smaller amplitudes (less than  $\sim 50\%$ ), the green curves provides a reasonable approximation of the flux ratio.

One noticeable feature of isobaric fluctuations is that around 2 keV, which is close to the average temperature in M87, the ratio  $\frac{\delta F_h}{F_h} / \frac{\delta F_s}{F_s}$  is close to zero. This is because, for the hard (3.5–7.5 keV) band,  $\frac{d \log \Lambda}{d \log T} \sim 2$  at

$T \sim 2$  keV and so  $\frac{\delta F_h}{F_h} \sim 0$ . The 3.5–7.5 keV image is

therefore a good proxy for density fluctuations produced by non-isobaric fluctuations (Forman et al. 2007), i.e., it is only sensitive to adiabatic and isothermal fluctuations. In contrast, for the 1.0–3.5 keV band the emissivity is essentially independent of temperature, as noted before.

Thus  $\frac{d \log \Lambda}{d \log T} \sim 0$  and  $\frac{\delta F_s}{F_s} \sim 2x$ . Therefore this band is

<sup>7</sup> This list is by no means complete, but for the sake of simplicity we concentrate on these three processes.

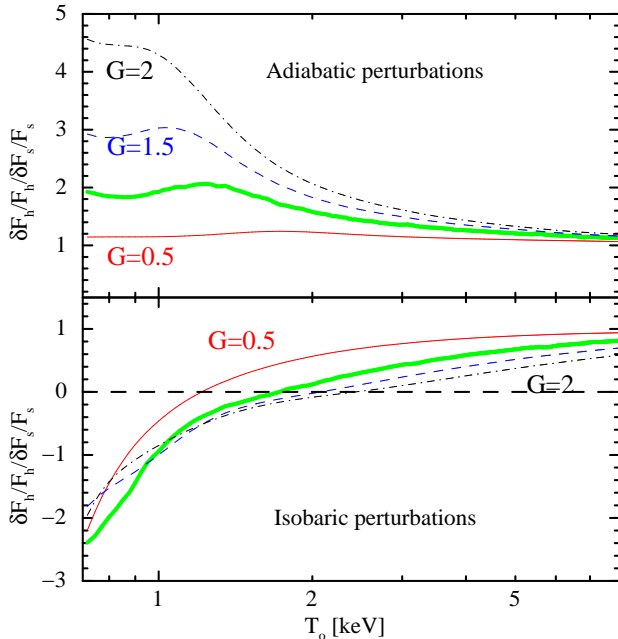


FIG. 1.— Ratio of relative amplitudes of flux fluctuations in the “hard” (3.5–7.5 keV) and “soft” (1.0–3.5 keV) bands as a function of initial temperature  $T_0$ , for adiabatic processes (top panel) and isobaric processes (bottom panel). A factor  $G$  (see Eq.1) characterizes the amplitude of the density fluctuation. The thick green line in each plot corresponds to a limit small density fluctuations ( $G - 1 \ll 1$ ), while the thin lines correspond to fluctuations with a given finite amplitude, as labeled in the plot. For the typical gas temperatures in M87 ( $T \sim 2$  keV) the amplitudes for isobaric and adiabatic processes differ strongly, opening the possibility to use this difference to distinguish these processes in *Chandra* images.

a proxy for density variations independently of the type of process that produces them. Figure 2 shows a soft (0.5–3.5 keV) and a hard (3.5–7.5 keV) image. The arms disappear in the hard band image, consistent with an isobaric nature interpretation, while the rings appear as larger amplitude surface brightness fluctuations in the hard band than in the soft band image, as expected for adiabatic weak shocks.

As is clear from Fig. 1 the ratio  $\frac{\delta F_h}{F_h} / \frac{\delta F_s}{F_s}$  for isobaric fluctuations changes sign around 2 keV and is also sensitive to the amplitude of fluctuations. Therefore one might expect to find either correlation or anti-correlation of fluxes in these two bands, although the absolute value of this ratio for isobaric fluctuations remains significantly smaller than for isothermal or adiabatic fluctuations.

### 3. POWER SPECTRA

We now proceed with the analysis of scale-dependent fluctuations, including faint ones, which we would like to characterize in a statistical sense through the power spectra and cross power spectra of two *Chandra* images. We will focus on fluctuations around the large scale intensity profile of the cluster by first dividing the images by the projected spherically symmetric  $\beta$ -model which best fits the azimuthally-averaged radial profile. The fluctuation images  $I = \frac{I_{raw}}{I_\beta} - 1$  in each energy band are used in the analysis below. Here  $I_{raw}$  is the original image and  $I_\beta$  is the symmetric  $\beta$ -model. The values of the slope  $\beta$  and core radius  $r_c$  of the  $\beta$  models fitted to the image in each

band are given in Sec. 5.

We will use the method described in Arévalo et al. (2012) to filter the fluctuation images in different spatial scales in order to calculate the power and cross spectra. This method corrects for gaps and irregular boundaries in the images. The 2D power spectrum can be converted into a 3D power spectrum through the de-projection procedure explained in Churazov et al. (2012) and finally converted into the amplitude of fluctuations in 3D as  $A_{3D} = \sqrt{P_{3D} * 4\pi k^3 / 2}$ , where  $k$  is the inverse of the spatial scale in units of  $\text{arcsec}^{-1}$ , and  $P_{3D}$  is the power per mode in the 3D power spectrum of emissivity fluctuations, reconstructed from the observed 2D power spectrum. Note that we use  $k = 1/l$  where  $l$  is the spatial scale, without the usual factor of  $2\pi$  in this relation. The factor 2 in the above expression is used to recast the amplitude in terms of linear density fluctuations instead of volume emissivity variations, since X-ray flux scales as  $\propto \rho^2$  and for small fluctuations this approximates to  $\rho^2 / \rho_o^2 = (1 + x)^2 \sim 1 + 2x$  where  $\rho_o$  is the unperturbed density and  $x$  is the density fluctuation. The cross spectra  $P_{1,2}$  are calculated using a similar procedure, by filtering the soft and hard band images with the Mexican hat filter, multiplying the filtered images in two bands by each other and calculating the mean value over all pixels.

In the discussion below, we assume that fluctuations, associated with adiabatic, isobaric and isothermal processes are spatially uncorrelated (in 3D). This assumption simplifies the interpretation of the results by removing all cross-terms for different types of fluctuations. While one can easily imagine a situations when different types of processes are correlated (e.g., buoyant bubbles are often accompanied by cool entrained gas), the procedure described below should be able to establish which type of process dominates the fluctuations in the images in a statistical sense.

#### 3.1. Correlation coefficient

Since the relative amplitudes of the soft and hard band fluctuations differ for different processes, fluctuations observed in two energy bands are expected to perfectly match each other (i.e.  $I_1 = \alpha I_2$ , where  $\alpha$  is a constant) only if the observed fluctuations are dominated by one particular type of process. To this end, a handy quantity is the correlation coefficient, which verifies if fluctuations in one band are linearly related to the fluctuations in another band. Given two fluctuation images, the correlation coefficient  $C_M$  can be computed as

$$C_M = \frac{\sum I_1 \times I_2}{\sqrt{\sum I_1^2 \times \sum I_2^2}}, \quad (4)$$

where the subscript  $M$  refers to the measured value as opposed to the predicted value. In practice, we calculate a scale dependent correlation coefficient  $C_M = \frac{P_{1,2}}{\sqrt{P_1 P_2}}$ , where  $P_1$ ,  $P_2$  and  $P_{12}$  are the power spectra of  $I_1$ ,  $I_2$  and their cross spectrum, respectively. The contribution of the Poisson noise to  $P_1$ ,  $P_2$  is removed by generating several images of Poisson fluctuations around the fitted  $\beta$ -model, calculating their power spectra and averaging the results. The averaged Poisson noise power spectrum

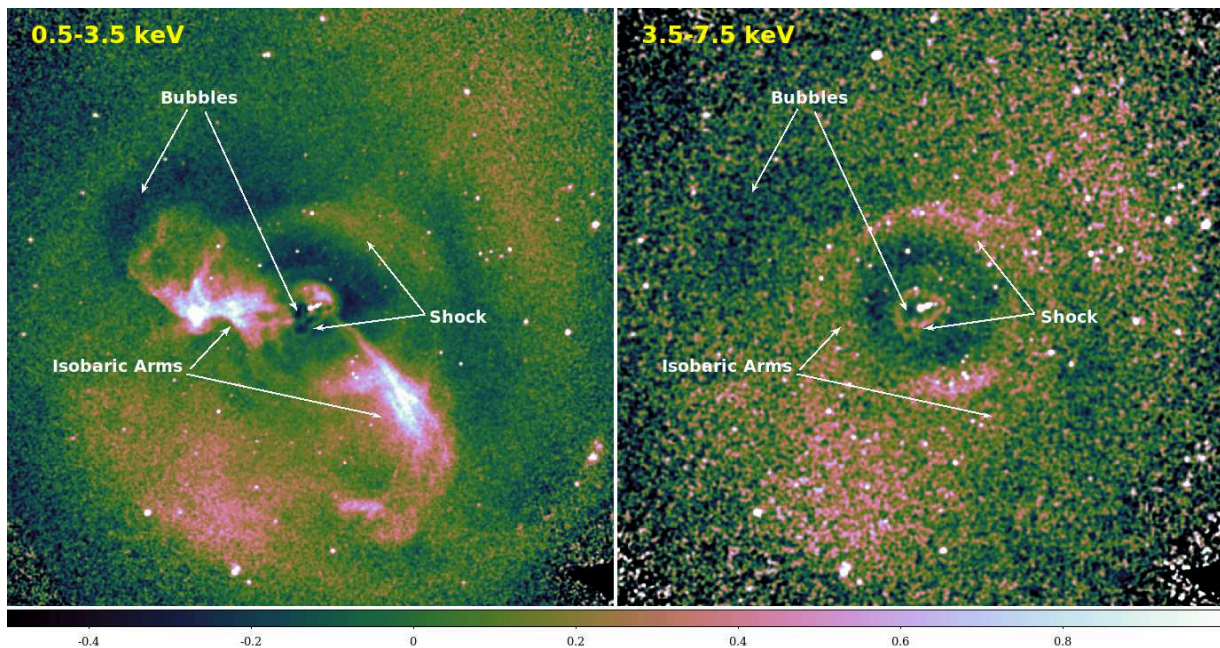


FIG. 2.— 0.5–3.5 keV and 3.5–7.5 keV images of M87 divided by their best-fitting  $\beta$ -models. The 0.5–3.5 keV image shows complicated substructure, while the 3.5–7.5 keV looks strikingly different. As shown by Forman et al. (2007), for gas temperatures, characteristic for M87, the surface brightness in this band is insensitive to isobaric fluctuations, but reflects projected pressure fluctuations. The lack of prominent “arms” in this image suggests that they are in pressure equilibrium with the ambient gas.

is then subtracted from  $P_1$  and  $P_2$ . Unlike the standard definition of the correlation coefficient in signal processing, we keep the sign of correlation coefficient, i.e. the allowed range of  $C_M$  is between -1 and 1, to differentiate correlated from anti-correlated fluctuations.

For a single type of process with small amplitude fluctuations in an isothermal cluster, the image in one band is just a linear transformation of the image in the other. Therefore, the correlation coefficient should be 1 or -1. In reality, clusters might be perturbed by different processes with comparable amplitudes. Some of these will have larger responses in the hard band than in the soft band and some other, spatially uncorrelated fluctuations, will have the opposite effect, so that the final images in both bands might also appear uncorrelated. This mixture of processes will be reflected in the measured correlation coefficient.

For a combination of different (independent) processes, the fluctuation image in band  $b$  can be expressed as  $I_b \propto \sum \alpha_{b,i} X_i$ , where  $X_i$  is proportional to the line-of-sight emission measure fluctuation relative to the unperturbed model, associated with the process  $i$ , and  $\alpha_{b,i} = \left(2 + \eta_i \frac{d \log \Lambda_b}{d \log T}\right)$  is the response in band  $b$  to this fluctuation. The expected correlation coefficient between soft and hard band images is then:

$$C_E = \frac{\sum_i \alpha_{1,i} \alpha_{2,i} \langle X_i^2 \rangle}{\sqrt{\sum_i \alpha_{1,i}^2 \langle X_i^2 \rangle \times \sum_j \alpha_{2,j}^2 \langle X_j^2 \rangle}}, \quad (5)$$

where the cross terms  $\langle X_i X_j \rangle$  have been dropped by the assumption of uncorrelated variations. It is clear from this equation that if a single process dominates the density fluctuations, e.g.  $\langle X_i^2 \rangle \gg \langle X_j^2 \rangle$  for all  $j$  and all  $\alpha_{1,i}$  and  $\alpha_{2,i}$  are of the same order, then the correlation coefficient converges to  $C_E = \frac{\alpha_{1,i} \alpha_{2,i}}{|\alpha_{1,i} \alpha_{2,i}|}$ , i.e., to a value of 1 or -1. On the other hand, for a mixture of processes with comparable amplitudes, the correlation coefficient takes a value  $|C_E| < 1$ , that can be predicted once the values of  $\alpha$  are known.

Notice, that  $C_M$  will be poorly constrained if the leading process does not produce a strong signal in one of the bands (i.e. if the response in  $I_1$  or  $I_2$  to this process is close to zero). For  $T = 2$  keV gas, this is the case for isobaric processes in the 3.5–7.5 keV band (see Fig. 1). As is clear from this figure, even for small variations of temperature around 2 keV, the sign of the ratio of amplitudes changes, leading to large uncertainty in the value of the correlation coefficient.

### 3.2. Relative amplitudes of soft and hard band fluctuations

Another useful quantity is the relative amplitudes of fluctuations in two energy bands  $R$ . The correlation coefficient  $C$  defined above in Eq. 4 equals the cross spectrum normalized by the variance of both bands. To estimate the relative amplitude of fluctuations,  $R$ , we normalize

the cross spectrum by the variance of the soft band only,

$$R = \frac{P_{1,2}}{P_1} = C \times \frac{\sqrt{P_2}}{\sqrt{P_1}}. \quad (6)$$

$R$  is proportional to the correlation coefficient and to the ratio of the amplitudes of the fluctuations in the hard and soft bands. The fact that we multiply the simple ratio of powers by the correlation coefficient preferentially highlights the ratio of correlated (or anti-correlated) fluctuations, which are the ones revealing we wish to study. We use the form  $\frac{P_{1,2}}{P_1}$  to calculate this quantity rather than  $C \times \frac{\sqrt{P_2}}{\sqrt{P_1}}$  because the first expression removes much of the uncertainty related to subtracting Poisson noise, which is high in the hard band. Since this noise is uncorrelated in the two bands, the Poisson noise cancels out in the cross term  $P_{1,2}$ , and the denominator only includes the soft band power  $P_1$  which has a lower Poisson noise level.

### 3.3. $R - C$ map

In the case of two or three types of independent fluctuation processes being comparably important, we expect that the relative amplitudes and the correlation coefficient of the soft and hard band images will have intermediate values.

Figure 3 shows the expected correlation coefficient (magenta contours) and amplitude ratio (blue contours) for the simulated images in the 1–3.5 keV and 3.5–7.5 keV bands. The top figure is calculated for an unperturbed temperature  $T_0 = 2$  keV and the bottom figure is for  $T_0 = 1.6$  keV. We normalize the total variance of density fluctuations, i.e., the sum of the variances corresponding to isobaric, adiabatic and isothermal processes, to 1. Therefore, in 3D Cartesian space, where the amplitude of each type of fluctuation corresponds to one of three orthogonal axes, the parameter space considered here corresponds to one octant of a spherical shell, which we project into the (x,y) plane. The amplitude of adiabatic fluctuations increases towards the right, isobaric fluctuations upwards and isothermal fluctuations decrease with increasing distance to the origin  $z = \sqrt{1 - (x^2 + y^2)}$ , so that pure adiabatic fluctuations are mapped into the bottom right corner, pure isobaric in the top left and pure isothermal to the origin. The correlation coefficient and amplitude ratio contours form an almost orthogonal patterns in these  $R - C$  maps. Therefore, for our idealised model of three uncorrelated processes, it is possible to find the coordinates of the intersection of the relevant  $R$  and  $C$  contours and from these to determine the fraction of the total variance produced by each type of density fluctuation. These unperturbed temperatures,  $T_0 = 1.6$  and  $T_0 = 2$  keV were chosen to bracket the average temperature in M87 within  $6'$  from the centre, which is the area that will be studied below. For the real cluster, or simulations calculated using the real cluster temperature radial profile, the measured  $R$  and  $C$  coordinates should lie between the limiting maps shown in Fig. 3.

## 4. TESTING $R$ AND $C$ WITH SIMULATED IMAGES

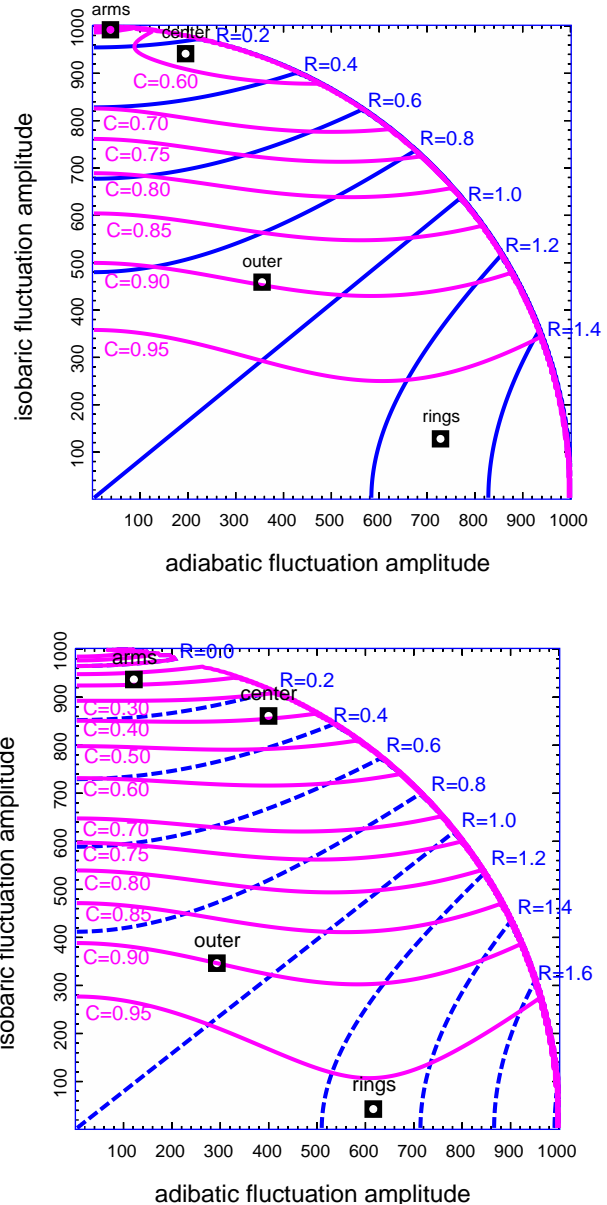


FIG. 3.—  $R$ - $C$  maps: Predicted correlation coefficient  $C$  (magenta contours) and  $R$  (blue contours) for a mixture of adiabatic, isobaric and isothermal processes, calculated assuming small-amplitude uncorrelated fluctuations of the three processes. The total variance of all three processes is normalised to unity. The amplitude of adiabatic fluctuations increases towards the right, isobaric fluctuations upwards and isothermal fluctuations decrease with increasing distance from the origin. The plot on the top shows the predicted values for an unperturbed temperature  $T_0 = 2$  keV and the plot on the bottom assumes  $T_0 = 1.6$  keV. These two temperatures bracket the range of temperatures observed for M87 in the radial range  $0.5 - 5'$ . Boxes schematically show the typical values of  $R$  and  $C$  calculated for several regions in M87. The “arms” and the “center” regions are clearly dominated by isobaric fluctuations. On the contrary, the circular “ring” is dominated by adiabatic fluctuations. The outer region (see Sec. 5.3 below) is consistent with a mixture of several processes, with isothermal fluctuations making the largest contribution.

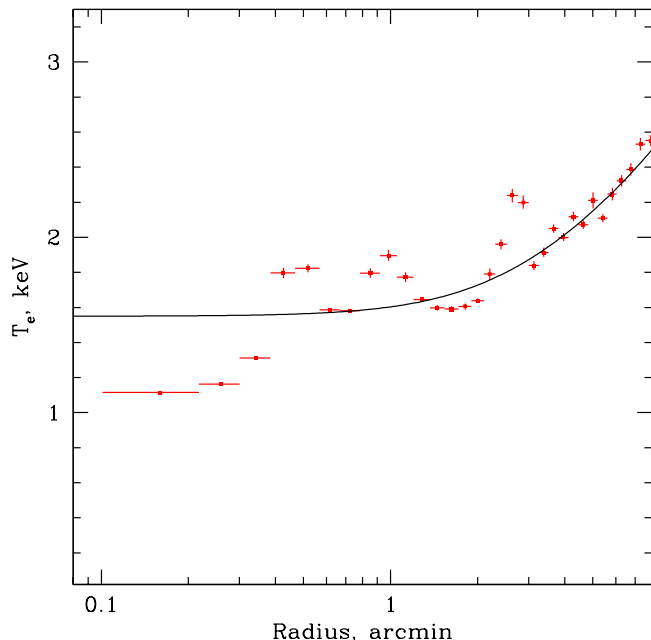


FIG. 4.— Azimuthally-averaged radial profile for the deprojected temperature in M87 from Churazov et al. (2008).

Even in the simplest scenario, when all fluctuations in the ICM correspond to only one type of process, other complications remain, e.g., radial variations of the mean temperature profile, projection effects and, possibly, non-linear responses to large-amplitude fluctuations. Even though the temperature profile is known, the location of each individual fluctuation along the line of sight is not. The latter effect can be corrected for only in a statistical sense. We proceed by testing the effect of radial temperature profiles and different amplitudes of fluctuation on  $R$  and  $C$  with simulated cluster images using the de-projected radial temperature profile for M87 from Churazov et al. (2008), shown in Fig. 4.

The images are produced by generating three independent realizations of the density fluctuation patterns (one for each of the three processes) as  $\rho_i/\rho_0 = e^{\delta_i}$ , where  $\delta_i$  is a Gaussian random field with a given 3D power spectrum  $P$ , representing fluctuations for process  $i$ . This log-normal form is used to allow for relatively large amplitude density fluctuations. The temperature fluctuations  $T_i/T_0$  are calculated for each process separately, e.g.  $T_i/T_0 = (\rho_i/\rho_0)^{2/3}$  for an adiabatic process. These values are then used to calculate the fluctuation of the volume emissivity  $e_i/e_0 = \frac{\rho_i^2 \Lambda_b(T_i)}{\rho_0^2 \Lambda(T_0)}$ . The final value of the emissivity in each band is calculated as  $e = e_0 \sum_{i=1}^3 \frac{e_i}{e_0}$ . The resulting 3D cubes are projected onto one plane to produce simulated images in each band. For these tests we assume, for each process, the same shape of the power spectrum  $P \propto k^{-3}$ , where  $k$  is the wavenumber. The choice of a  $k^{-3}$  spectrum is rather arbitrary. It has the advantage that in 3D it corresponds to the same am-

plitude at all scales and is not far from the canonical Kolmogorov slope of  $k^{-11/3}$ , which is consistent with the observed spectrum in M87 and Perseus (Zhuravleva et al. 2014).

The soft (1.0-3.5 keV) and hard (3.5-7.5 keV) band simulated images are processed in the same way as real images (see §5 below), except for the correction for Poisson noise. Namely, we fit  $\beta$ -model to each image, divide the image by the  $\beta$ -model and calculate  $C$  and  $R$  over a range of angular scales.

In the following two subsections (§4.1 and §4.2) we perform this analysis for pure adiabatic or pure isobaric fluctuations, varying their amplitudes and assuming either an isothermal cluster or one with a radial temperature profile. Isothermal fluctuations are not considered separately, since they have the same impact on the emissivity in all bands, so the emissivity patterns and images are identical in all bands, except for the overall radial temperature profile which largely cancels out by fitting and dividing the images by the projected  $\beta$ -model. In § 4.3 we consider a mixture of all three processes.

#### 4.1. Pure adiabatic fluctuations

Figure 5 summarizes the results of simulations for pure adiabatic fluctuations. Left and right columns correspond to a cluster with a radial temperature profile and to an isothermal cluster, respectively. Top and bottom rows are for large and small amplitudes<sup>8</sup>, respectively. The top section in each plot shows the spectra of the recovered amplitudes in the soft (red) and hard (blue) bands. In the middle sections we plot the correlation coefficient  $C$ , and the pink line in the bottom panel shows the ratio  $R$  as defined in eq. 6. The dashed line shows the expected value of  $R$  for an adiabatic process at an unperturbed temperature  $T_0 = 2$  keV.

For adiabatic fluctuations we can conclude that, for these temperatures and energy bands, the correlation coefficient  $C$  is in the range 0.95–1, and  $R$  is between 1.5 and 2, even for a varying temperature profile and for large or small fluctuations. Large fluctuations introduce a trend in the value of  $R$ , where hard band fluctuations increasingly dominate towards smaller spatial scales, but their value remains in the range expected for an adiabatic process. Therefore, pure adiabatic fluctuations should be clearly identifiable in the data by their very high correlation coefficient and large amplitude ratio,  $C \sim 1$ ,  $R > 1$ .

For a temperature of 2 keV the expected value of  $R$  for adiabatic fluctuations is  $\sim 1.6$  (see horizontal dashed line in Fig. 5). Note that for the temperature profile adopted here (see Fig. 4), the temperature is about 1.7 keV over a significant part of the simulated volume. The green curves in the top panel in Fig. 1 show that for this temperature, the expected ratio of amplitudes is closer to 1.8, in excellent agreement with the  $R$  value of these simulations. This explains why the recovered value of  $R$  is larger in the left column of Fig. 5, which uses a more realistic temperature profile.

<sup>8</sup> Since our simulated box has finite size, the projected surface brightness distribution does not correspond to a perfect  $\beta$ -model. This causes a hump in the amplitude on the largest scales, comparable to the size of the box.

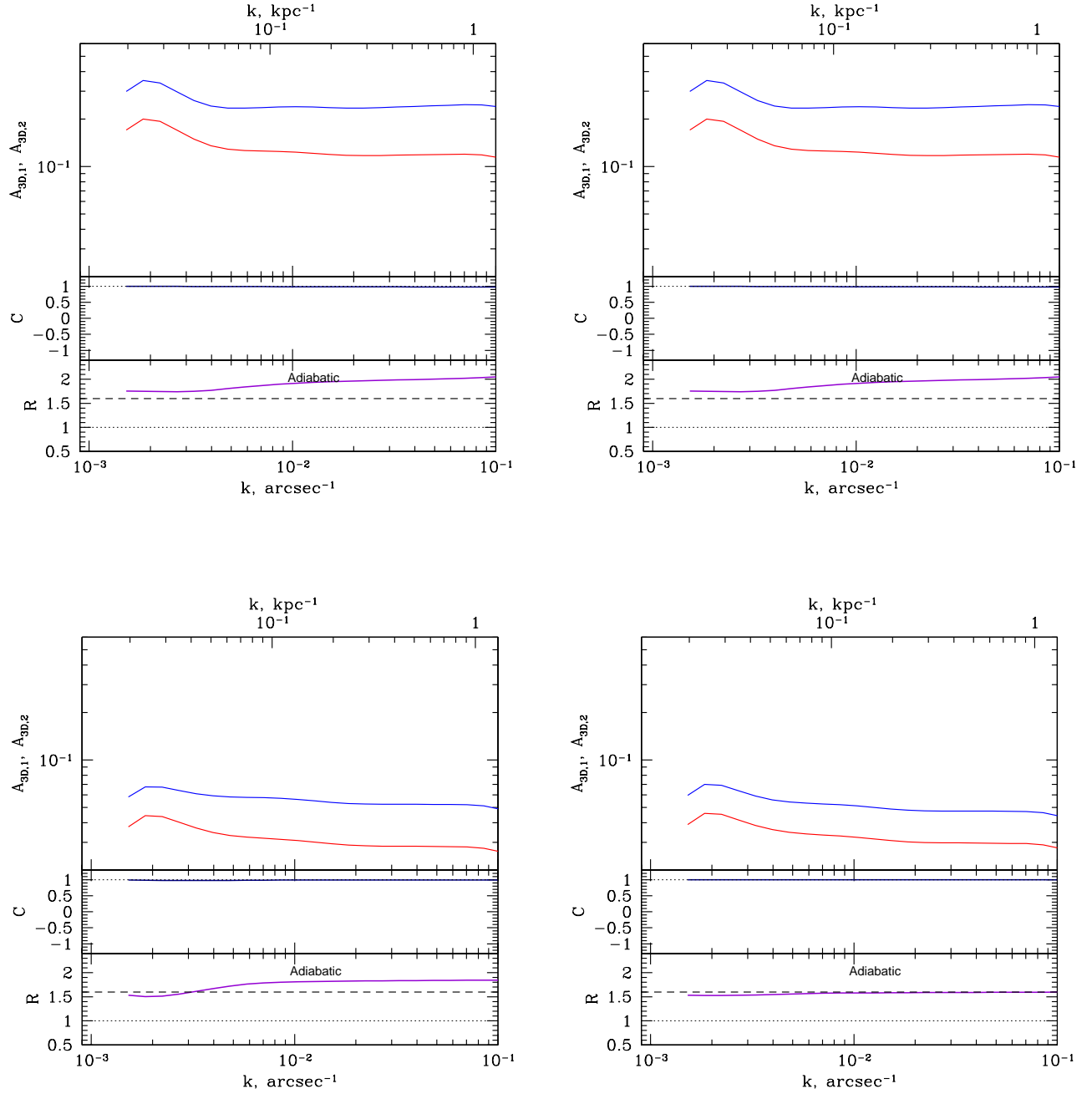


FIG. 5.— Test of the recovered  $C$  and  $R$  values for simulated images with pure adiabatic fluctuations. Left: Average radial temperature profile as measured for M87. Right: isothermal cluster at  $T = 2$  keV. The top panels correspond to large amplitude fluctuations and the lower panels to lower amplitudes. The amplitude of the fluctuations observed in M87 has intermediate values. In the top section of each panel, the blue and red lines show the hard and soft amplitude spectra, respectively. In the middle section, solid blue lines show the correlation coefficient  $C$  and in the bottom section the solid purple lines show the relative amplitude  $R$ . Pure adiabatic fluctuations show high correlation coefficient  $C$  and high value of  $R > 1$ . The dashed lines in the bottom panel mark the expected value of  $R$  for adiabatic fluctuations around  $T_0 = 2$  keV.

#### 4.2. Pure isobaric fluctuations

The situation is more complex for isobaric fluctuations. As can be seen in Fig. 1, the hard band response is close to zero in the temperature range of interest, i.e. isobaric density fluctuations might show up clearly in the soft band but be weak or absent in the hard band. Additionally, the response in the hard band changes from positive to negative values as the temperature fluctuates around  $\sim 2$  keV and this critical temperature also depends on the amplitude of the fluctuations. Therefore, the hard band response depends sensitively on the amplitude of the fluctuations and on the local unperturbed temperature, which can produce correlated, anti-correlated or apparently unrelated fluctuations in the soft and hard band images.

Fig. 6 shows the same simulations as in Fig. 5 but for pure isobaric fluctuations. In all cases, the hard band amplitudes are smaller by a factor of a few than in the soft band, and the amplitude ratio is low, as expected. Very small fluctuations around  $T_0 = 2$  keV (bottom right panel) remain in the positive response range and the correlation coefficient remains high and positive. Large amplitude fluctuations on the other hand, produce a negative hard band response, so the fluctuations can be highly anti-correlated. For the left panels, which are simulated using the radial temperature profile of Fig. 4, the majority of the simulated region is within  $6'$  from the centre and therefore has a temperature lower than 2 keV, producing mostly anti-correlated hard and soft fluctuations.

Isobaric fluctuations can be identified more reliably through the low amplitude of the hard band fluctuations ( $|R| \ll 1$ ), while the correlation coefficient must be interpreted with care, considering the amplitude of the fluctuations and the local unperturbed temperature, although small ( $C \sim 0$ ) and negative values of  $C$  always correspond to isobaric fluctuations.

#### 4.3. Mixture of three processes

We now consider a combination of three different types of processes by combining the simulated images described above and including ‘isothermal’ simulated images as well, where the fluctuation amplitudes are the same in soft and hard bands. To construct the images we simply generate three patterns of density fluctuations (modulated by a global  $\beta$ -model), convert each pattern into soft and hard band emissivities, add the flux contributions from the three processes in each volume element and project onto one plane. We measure the correlation coefficient  $C$  and the ratio  $R$  of each pair of images and compare these values with the  $R - C$  maps, derived for an isothermal cluster and linear fluctuations. As before we use simulated images in the 1–3.5 keV and 3.5–7.5 keV bands and vary the relative amplitudes of the three processes in independent runs.

The relative contributions of the three processes in the simulated images were chosen to cover several limiting cases: each single process dominating, equal contributions of two processes and equal contributions from the three processes. The positions corresponding to these setups are marked with crosses in Fig. 7, with single processes marked in red, green and cyan. Two equal-

amplitude processes cases are marked in yellow, black and white, and the case where the three processes have equal amplitudes is marked in blue. We then processed each pair of simulated images as we would do with the real data. We calculated  $R(k_{ref})$  and  $C(k_{ref})$  values for each pair and plotted the resulting values as contours in blue and magenta in Fig. 7. Here we choose  $k_{ref} = 10^{-1}$  kpc, corresponding to the middle of the range of scales we probe in M87. The intersection of the contours yields the recovered values of relative amplitudes of the adiabatic, isothermal and isobaric process. These intersections are marked with ellipses in the same color as the corresponding input parameters that are marked with crosses.

The  $R - C$  map, that we use to compare the outcome of the simulations, was calculated for small-amplitude fluctuations around a constant temperature  $T_0 = 1.6$  keV, which is representative of the unperturbed temperature range used in the simulations. The results show that, even in the presence of a global temperature gradient, the leading type of fluctuation is correctly recovered by comparing the measured values of  $C$  and  $R$  with the predictions for a constant temperature cluster. Indeed, for the majority of cases the recovered characteristics of fluctuations (ellipses in Fig. 7) are close to the input values (crosses in Fig. 7). For a combination of two or more processes the accuracy deteriorates but the dominating processes and their relative fractions can still be qualitatively recovered.

We note that the relative responses of both bands are sensitive to the amplitude of fluctuations when the unperturbed temperature is low (see low  $T_0$  range in Fig. 1). In this case large amplitude fluctuations can lead to  $R$  values that fall outside the range of the  $R - C$  maps in Fig. 3 that was calculated assuming small-amplitude fluctuations. Large-amplitude adiabatic fluctuations will simply produce larger  $R$  values than those predicted for the pure adiabatic case (right corner of the  $R - C$  map), while large isobaric fluctuations can have  $R$  values smaller than the minimum predicted for small-amplitude fluctuations (top left corner of the map). Nevertheless, even for large-amplitude fluctuations, adiabatic and isobaric fluctuations remain well-separated in the  $R - C$  map.

## 5. NATURE OF THE SURFACE BRIGHTNESS FLUCTUATIONS IN M87

We use archival *Chandra* observations of M87 with ObsIDs 2707, 3717, 5826, 5827, 5828, 6186, 7210, 7211, 7212 and 11783. The data were processed following the procedure described in Vikhlinin et al. (2005). The co-added final image has a pixel size of  $1''$  and fairly uniform total exposure of about 420 ks within  $7'$  in radius of the centre, which is the area we will use for the following analysis. The well studied X-ray jet (e.g., Marshall et al. 2002; Harris et al. 2003) and the point sources, mainly corresponding to X-ray binaries (Jordán et al. 2004), contaminate the signal from the ICM fluctuations and were excised from the images before further analysis.

We use X-ray images of M87 in the 1–3.5 keV and 3.5–7.5 keV bands to calculate the power and cross-power spectra of fluctuations, the correlation coefficient  $C$  and



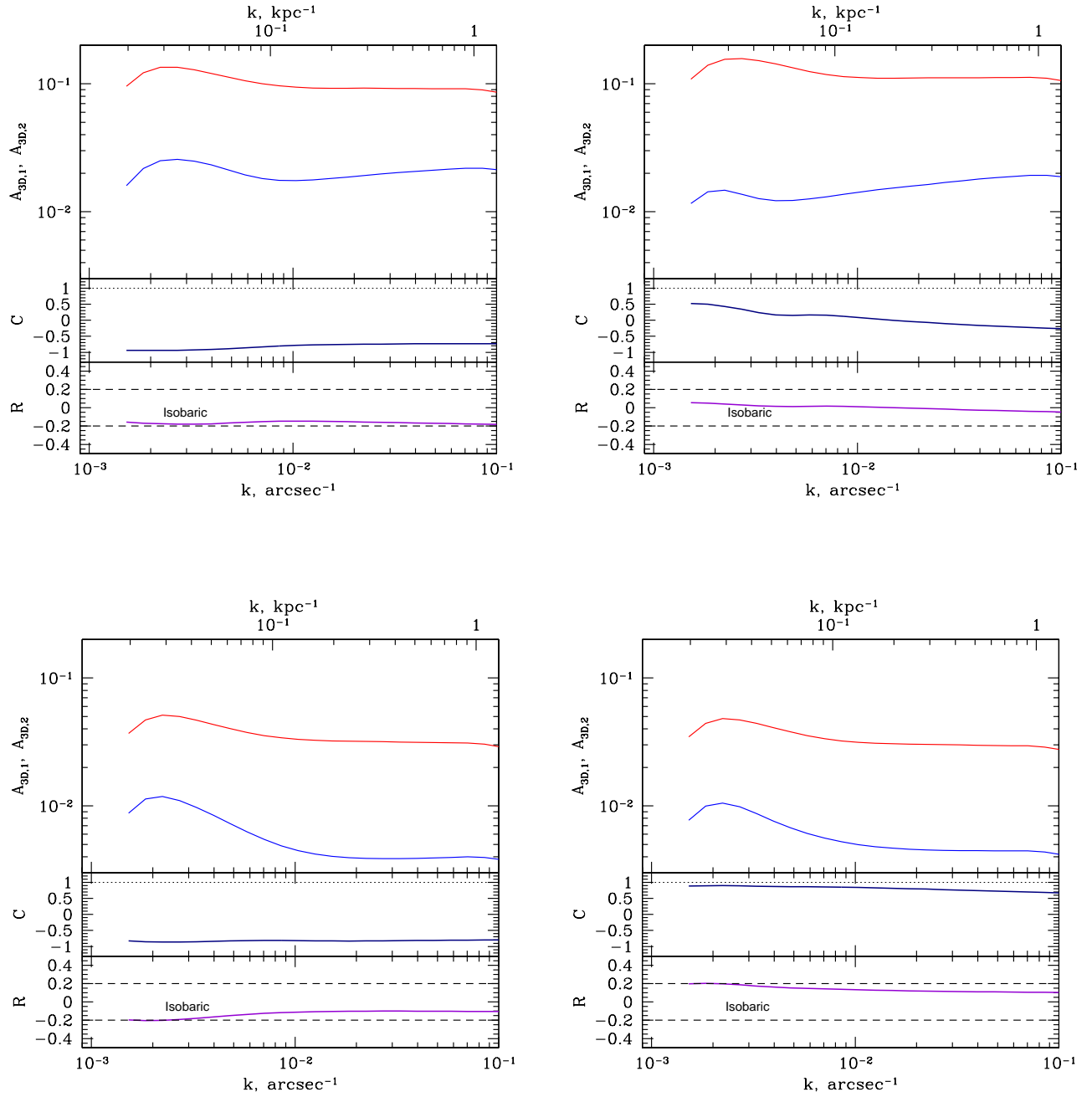


FIG. 6.— The same as in Fig. 5 but for pure isobaric fluctuations. As expected, pure isobaric fluctuations lead to low values of  $R < 1$  and small (or even negative) correlation coefficient  $C$  (except for the case of a perfectly isothermal cluster and very small fluctuations). The dashed lines in the bottom panel mark the range of values of  $R$  expected for isobaric fluctuations around  $T_0 = 2\text{keV}$ .

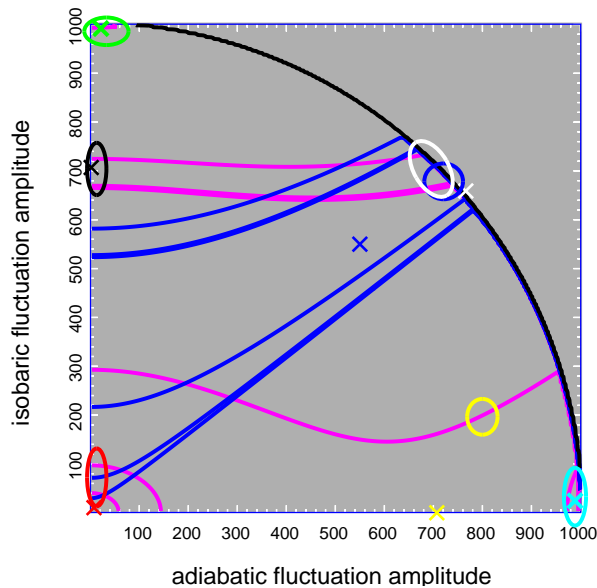


FIG. 7.— Simulated and recovered relative amplitudes of adiabatic, isobaric and isothermal fluctuations for 7 pairs of simulated images. Input values are marked with crosses. Blue and magenta lines show the contours, corresponding to  $C$  and  $R$  value obtained from the simulated images. The intersection of these contours define the recovered values of relative amplitudes of adiabatic, isobaric and isothermal fluctuations. These intersections are shown with ellipses (same color as the input values). When a single process dominates the density fluctuations, the recovered values are close to the input values. For a combination of two or more processes the accuracy deteriorates but the dominating processes and their relative fractions are qualitatively recovered.

the amplitude ratio  $R$ . We fit  $\beta$ -models to the images in each energy band and then divide the images by these models to remove the large scale symmetric structure. The best fitting  $\beta$ -model parameters are  $R_c = 0.23'$  and  $\beta = 0.37$  for the 1–3.5 keV image and  $R_c = 0.03'$  and  $\beta = 0.30$  for the 3.5–7.5 keV image. The smaller value of  $\beta$  for the hard band reflects the global radial temperature increase that makes the hard band image less peaked. The resulting “flattened” images are shown in Fig. 2.

We first calculate the amplitude and cross spectrum for the entire region, masking out only point sources and the jet. This region of the ICM is perturbed by different processes so our aim is to establish whether one of these clearly dominates the fluctuations in the cluster. The resulting spectra are shown in Fig. 8. The amplitude spectra in the top panel show a very slight dependence of amplitude with spatial scale. Perfectly horizontal amplitude spectra correspond to a 3D power spectrum  $P_{3D} \propto k^{-3}$  so this slight decrease of amplitude with  $k$  indicates a slightly steeper  $P_{3D}$ . This is consistent with the power spectral slope obtained for M87 by Zhuravleva et al. (2014), although in that paper the arms structure was excluded from the analysis making the amplitudes smaller, and for the Perseus cluster by Zhuravleva et al. (2015). The small  $R$  and  $C$  values reveal the strong contribution of isobaric processes to the fluctuation pattern of this region. For spatial scales of about  $100''$  we find  $R = 0.35$  and  $C = 0.5$ . This value of  $R$  occurs only at the top left corner of the  $R - C$  maps

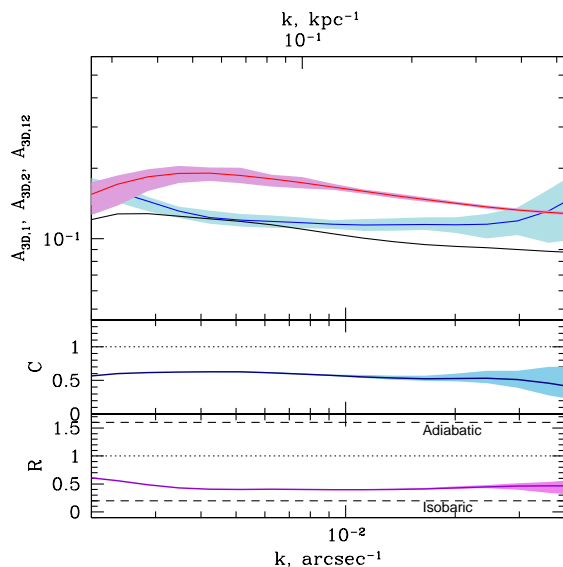


FIG. 8.— Power and cross-power spectra, correlation coefficient and ratio  $R$  for the  $14' \times 14'$  Chandra images of M87 in the 1–3.5 keV and 3.5–7.5 keV bands. **Top panel:** power spectra of fluctuation images in the soft (red) and hard (blue) bands. Shaded regions show the uncertainty in the measured spectra. The cross-power spectrum between these bands is shown with the black solid line. **Middle panel:** correlation coefficient  $C$ . **Bottom panel:** amplitudes ratio  $R = P_{12}/P_1$ . The dashed lines mark the expected value of  $C$  for pure isobaric and adiabatic fluctuations, around  $T_0 = 2$  keV. The low values of  $R$  and  $C$  indicate that isobaric fluctuations account for 70–80% of the variance in this region. In the soft band the total variance is dominated by the contribution of filaments/arms of cool gas.

in Fig. 3, where isobaric fluctuations are responsible for about 70–80% of the total variance. In this corner, the coherence is very sensitive to the underlying temperature so we only remark that, as expected for both maps, the absolute value of the coherence should be significantly lower than 1 but its precise value is hard to predict.

We now proceed with the analysis of selected regions of the image. We identified structures which might be dominated by different processes. From Fig. 2 it is clear that the ring structures around  $3'$  from the centre correspond to adiabatic fluctuations (see e.g., Forman et al. 2007, where this structure is identified as a weak shock), while the arms stretching to the east and south-west are isobaric, since they do not appear in the hard band image. Guided by these arguments we subdivided the image into three regions: “arms”, “ring” and “outer”. We now extract the power spectra of these regions to verify if their  $R - C$  values match our expectations and establish the contribution of the different processes in regions with less prominent features.

### 5.1. Arms

The filamentary regions extending to about  $7'$  from the centre towards the east and south-west, the arms, were identified in the X-ray image of M87 by Bohringer et al. (1995) who pointed out their spatial correlation with similar structures seen in the radio band. In Churazov et al.

(2001), these structures were explained as gas entrained from the core region by rising buoyant bubbles of relativistic plasma. Later Molendi (2002) noted that these regions were significantly colder than the surrounding medium, and required a two-temperature model for the cluster, with temperatures as low as 0.8–1 keV for the arms. Forman et al. (2005) produced new temperature maps of the M87 cluster confirming the lower temperature of both arms while finding no strong difference in the metallicity of the gas in the arms compared to the surrounding medium.

The part of the M87 image selected for our analysis of the arms is shown in the left panel of Fig. 9. The width of the selected region is about  $130''$ , so we will restrict the analysis to wave numbers  $k > 8 \times 10^{-3} \text{ arcsec}^{-1}$ . The power spectra are shown in the left panel in Fig. 10. On the smallest scales, with  $k > 2 \times 10^{-2} \text{ arcsec}^{-1}$ , unresolved point sources make a significant contribution to the variance of the hard band image. Since the spectra of unresolved sources are typically much harder than the spectra of the M87 gas, these sources create an upturn in the hard band power spectrum and also affect the amplitude ratio and correlation coefficient. Since we are interested in the arm structures only, we restrict the analysis to  $k < 2 \times 10^{-2} \text{ arcsec}^{-1}$ . In this range of scales, the correlation coefficient and amplitude ratios are small with values of  $R \sim 0.1$  and  $C \sim 0.35$ , very similar to those of the entire image, so the same interpretation applies here, only shifting the relative importance of the isobaric fluctuations to even higher values. The corresponding region in the  $R - C$  maps is labeled ‘arms’ in Fig. 3.

The value of  $R \sim 0.2$  can be compared with the predictions for isobaric fluctuations plotted in the bottom panel in Fig. 1. For an initial temperature of  $T_0 \sim 2 \text{ keV}$ , small variations of density (green curve) will produce an amplitude ratio of this order of magnitude. Pure isothermal ( $R \sim 1$ ) and adiabatic processes ( $R > 1$ ) can be safely excluded, while isobaric fluctuations in these regions are completely consistent with the amplitude ratios.

### 5.2. Rings at $2-3.75' (11-17 \text{ kpc})$

The ring sections of increased surface brightness at radii of  $3-3.75'$  from the centre were first identified by Young et al. (2002) from *Chandra* images. Forman et al. (2005) present a temperature map of this region showing an increase in temperature at the rings, compared to the immediate surrounding gas, which together with the nearly circular appearance of the ring support its interpretation as a weak shock Forman et al. (see also 2007). Million et al. (2010) used deep *Chandra* images to confirm its weak shock nature.

The ring appears more prominent in the 3.5–7.5 keV band than in the softer bands, consistent with an adiabatic origin (top panel in Fig. 1). We calculated  $R$  and  $C$  for a section of the image covering the northern part of the ring, excising only the point sources from this region, as shown in the central panel in Fig. 9. The thickness of the section including the ring is about  $150''$ , so we will focus on size scales smaller or equal to this, with  $k > 6 \times 10^{-3} \text{ arcsec}^{-1}$ . As can be seen in the central panel in Fig. 10, around  $k = 10^{-2} \text{ arcsec}^{-1}$ ,  $C \gtrsim 0.95$  and

$R = 1.3$ . The temperature in this region is about 2 keV, so we should interpret the results using the top panel in Fig. 3. The location of the intersections of the corresponding contours suggests the following distribution of amplitudes of the contributing processes: adiabatic  $\sim 0.8$ , isobaric  $\sim 0.3$ , isothermal  $\sim 0.5$ . In terms of variance  $\sim 60\%$  of the total variance can be attributed to adiabatic processes,  $\sim 10\%$  of the variance to isobaric processes and  $\sim 30\%$  of the variance to isothermal processes. For higher mean temperatures, the adiabatic contribution would increase further. Therefore, adiabatic fluctuations dominate the variance in this region although there can be a non-negligible contribution from at least one other process.

### 5.3. Outer region

We now proceed with the analysis of the outer region shown in the right panel of Fig. 9, where the central  $2'$ , the arms and the shock have been excluded. The resulting power spectra for the 1–3.5 and 3.5–7.5 keV band images are shown in the right panel of Fig. 10 (see also Zhuravleva et al. 2014). We consider only scales  $\sim 100''$  and larger, i.e. below  $k = 10^{-2} \text{ arcsec}^{-1}$  since in this region the surface brightness is very low in the hard band and the power drops an order of magnitude below the Poisson noise level slightly above these scales. Around  $k = 10^{-2} \text{ arcsec}^{-1}$ , both  $C$  and  $R$  are about 0.9, pointing to a mixture of the three types of processes. For mean temperature  $T_0 \sim 2 \text{ keV}$ , the values  $R \sim 0.9$  and  $C \sim 0.9$  imply relative amplitudes of  $\sim 0.4$ , 0.4 and 0.8 produced by adiabatic, isobaric and isothermal processes, respectively. In terms of variance, the majority, about 70%, can be attributed to isothermal processes with the remaining  $\sim 30\%$  distributed equally between adiabatic and isobaric processes. For a lower temperature  $T_0 \sim 1.6 \text{ keV}$  the isothermal processes would have an even higher fraction of the total variance, although a temperature of 1.6 keV is probably too low for this outer region and the first estimate is more accurate. Since this region is larger than the previous two, we can also focus on fluctuations on larger scales. At  $k = 3 \times 10^{-3} \text{ arcsec}^{-1}$ , or correspondingly spatial scales of  $\sim 30 \text{ kpc}$ , both the coherence and the amplitude ratio drop, pointing to an increase in the relative amplitude of isobaric fluctuations.

Once the prominent structures such as the arms and weak shocks are excluded, the outer region appears to be dominated by isothermal fluctuations, at least for fluctuations on scales of  $\sim 10 \text{ kpc}$ . In our analysis, isothermal structures simply correspond to density fluctuations that produce equal amplitude fluctuations in the soft and hard band fluxes, such as, e.g., X-ray cavities produced by radio bubbles, or the global asymmetry of the cluster. The dominance of isothermal fluctuations of these scales in this region is consistent with the presence of several bubbles (see, e.g., Owen et al. 2000; Forman et al. 2007). In addition to these bubbles, at distances of about  $6'.7$  from the centre the gas is likely disturbed by large scale sloshing (e.g. Fig. 2 in Simionescu et al. 2010; Werner et al. 2015). The most prominent cold front presumably associated with sloshing is located  $\sim 20'$  north of M87. This feature is outside the region studied here. There is also a feature  $\sim 6'$  south of M87 (green area in the lower left

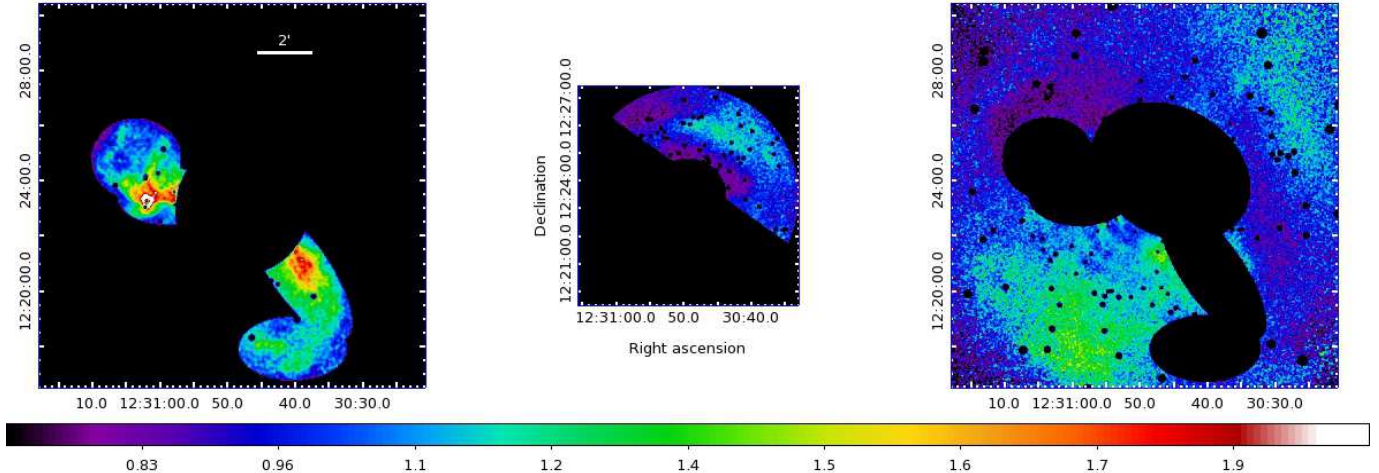


FIG. 9.— Selected image regions. Left: arms, center: shock, right: rest. The sections correspond to the same 1–3.5 keV image of M87, divided by the best-fitting  $\beta$ -model. All images are on the same scale. The size of the largest image is  $14' \times 14'$ .

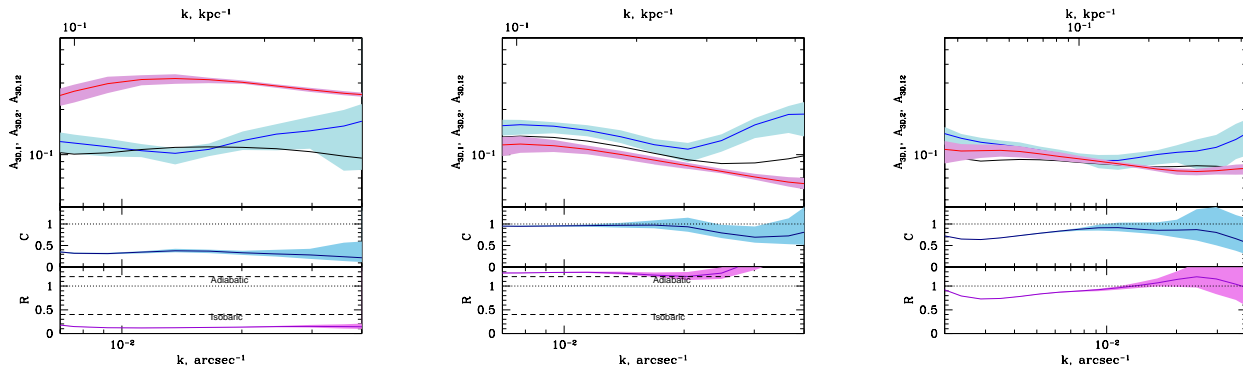


FIG. 10.— The same as in Fig. 8 for three separate regions shown in Fig. 9. **Left panel:** the region dominated by cool arms. The value of  $R$  is close to that expected for isobaric fluctuations around mean temperature  $T_0 = 2$  keV. The correlation coefficient is small, as expected. **Central panel:** the shock region. Two dashed black lines correspond to pure adiabatic and isobaric processes for 3 keV gas. The values of  $R$  and  $C$  suggest that adiabatic process (weak shock) dominates. **Right panel:** “outer” region (no arms, no central region, no shock) is only robust for  $k \lesssim 10^{-2} \text{ arcsec}^{-1}$  since there are very few counts in this region and the hard band power drops by an order of magnitude below the Poisson noise level. Around and below  $k = 10^{-2} \text{ arcsec}^{-1}$  both the correlation coefficient and ratio are below unity (see text for details).

quadrant of the right panel in Fig. 9) that might be a fainter counterpart of the more prominent northern cold front, similar to the structures predicted by 2D numerical simulations of gas sloshing, shown in the bottom panel in Fig. 11 in Churazov et al. (2003).

#### 5.4. Central $2'$

The central  $2'$  (radius) area appears disturbed by several processes so we study it separately. Fig. 11 shows this region in three energy bands: 0.5–1, 1–3.5 and 3.5–7.5 keV. Each image has been divided by its best-fitting  $\beta$ -model to remove the symmetric large scale structure and highlight the fluctuations, which are shown on the same colour scale. Almost all the bright features, especially the base of the arms toward the east and southwest, appear stronger in the softest band, indicative of their isobaric nature. A few areas, marked by the red arrows, however, appear brighter in the 1–3.5 keV band than in the 0.5–1 keV band, which points towards adiabatic

fluctuations. These regions include the “bud” structure identified by Forman et al. (2005, 2007) as a budding radio bubble. In the hard 3.5–7.5 keV band image (right panel of Fig. 11), only this inner ring structure is visible, suggesting an adiabatic nature of the rings and corroborating the isobaric nature of the base of the arms.

The central region is cooler than the rest of the cluster, as can be seen in the temperature profile in Fig. 4, averaging about 1.6 keV. For this low temperature, there are noticeable differences in the response to density fluctuations in the 0.5–1 keV and 1–3.5 keV bands, which we can exploit to study the origin of the fluctuations further. Figure 12 shows the amplitude ratios for adiabatic and isobaric density fluctuations, similarly to Fig. 1 but this time comparing the 0.5–1 keV and 1–3.5 keV bands. For unperturbed temperatures below 2 keV, the fractional amplitudes deviate strongly from unity, especially for isobaric processes.

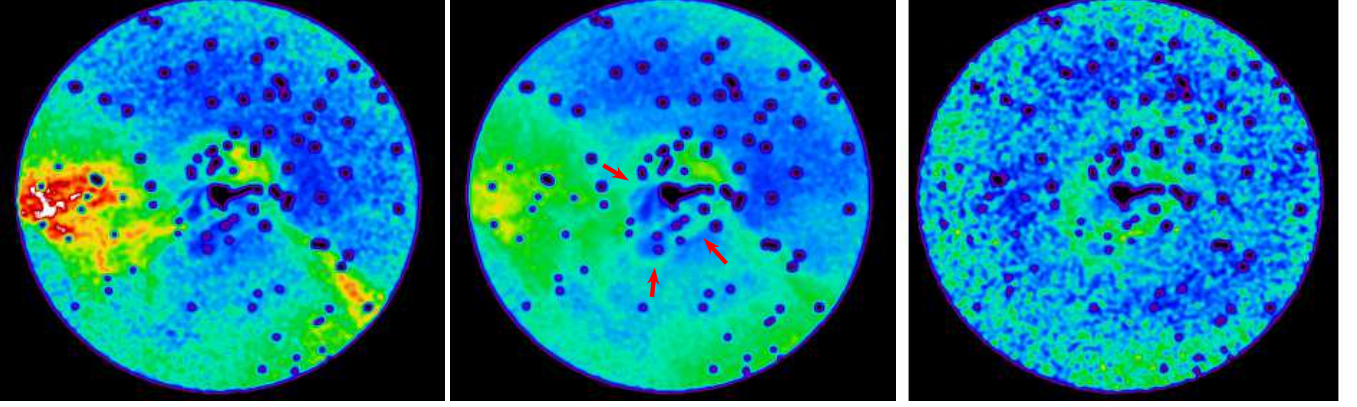


FIG. 11.— Central,  $2'$  radius region, from left to right: 0.5–1, 1–3.5 and 3.5–7.5 keV images, each divided by its best-fitting  $\beta$ -model. Note how the fluctuations corresponding to the base of the arms decrease with increasing energy while the ring structure (marked with red arrows in the central plot) becomes more dominant with respect to other feature with increasing energy. These trends are characteristic of isobaric and adiabatic fluctuations, respectively.

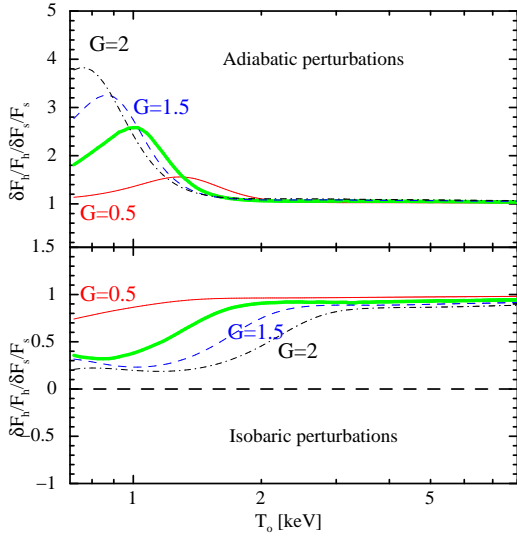


FIG. 12.— Amplitude ratios for 0.5–1 keV and 1–3.5 keV band images for adiabatic (top panel) and isobaric (bottom panel) processes, respectively. The fluctuations are modelled as density variations from an initial value  $\rho_o$  by a factor  $G$  ( $\rho = \rho_o * G$ ). At temperatures below 3 keV, these bands have amplitude ratios significantly different from unity. The adiabatic fluctuations appear significantly larger in the hard band, while isobaric fluctuations appear larger in the soft band. The thick green lines in each plot correspond to small amplitude fluctuations, while the thin lines correspond to larger (nonlinear) fluctuations as labeled in the figure.

The power spectrum analysis of the central region for the very soft 0.5–1 keV and soft 1–3.5 keV energy bands is shown in Fig. 13. The correlation coefficient is  $C \sim 0.9 - 0.7$  and  $R \sim 0.5 - 0.4$ . These value can be compared directly with the curves in Fig. 12. For an unperturbed temperature  $T_0 = 2$  keV, an amplitude ratio of 0.5 requires a factor of  $\sim 2$  density increase due to isobaric processes. If the unperturbed temperature is  $T_0 = 1.6$ , then the required density increase  $\sim 1.5$  is more modest. The correlation coefficient drops slightly towards smaller spatial scales (higher values of  $k$ ) hinting at uncorrelated fluctuations of a different type becoming stronger at smaller scales, probably the adiabatic inner ring structure marked with red arrows in Fig. 11.

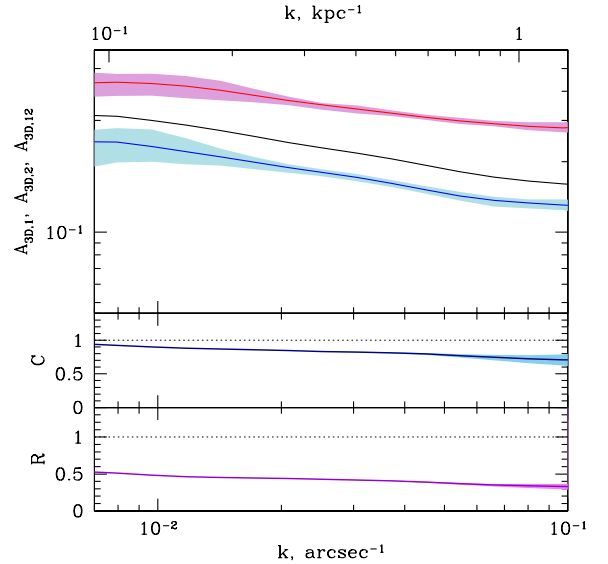


FIG. 13.— Top: Amplitude (red, blue) and cross spectrum (black) between 0.5–1 keV and 1–3.5 keV images, for the central region (left and central images in Fig. 11). Middle: correlation coefficient,  $C$ . Bottom: amplitude ratio  $R = P_{1,2}/P_1$ .  $R = 0.5$  is consistent with mainly isobaric fluctuations, where the density is lower than ambient by 10% if the ambient temperature is  $T_0=1.2$  keV (green line in Fig. 12), by a factor of 1.5 from an ambient temperature of 1.8 keV or by a factor of 2 from an ambient temperature of 2 keV (green, blue and black lines, respectively, in Fig. 12). The correlation coefficient  $C$  ranging from 0.7 to 0.9 is consistent with dominant isobaric fluctuations, contaminated by other processes.

For this region, we have also calculated the values of  $R$  and  $C$  for the images in the 1–3.5 and 3.5–7.5 keV energy bands (see Fig. 14). On scales  $\sim 2'$  (or equivalently  $\sim 9$  kpc), similar to the radius of this central region,  $C \sim 0.4$  and  $R \sim 0.3$ , which correspond to the top left corner of the  $R - C$  maps in Fig. 3, i.e. mostly isobaric fluctuations, confirming the result of the low energy bands. On scales of  $\sim 20''$ , about the thickness of the ring in the right panel in Fig. 11, the values of  $R$  and  $C$  both increase to  $\sim 0.5$ , corresponding to an increased contribu-

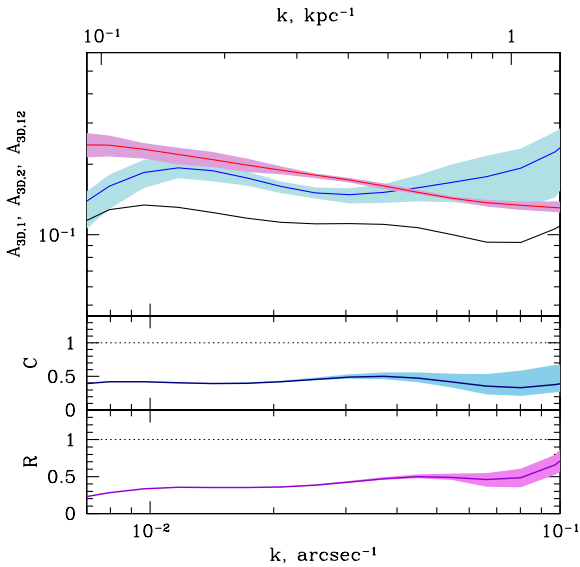


FIG. 14.— Top: Amplitude (red, blue) and cross spectrum (black) between 1–3.5 keV and 3.5–7.5 keV images, for the central region (central and right images in Fig. 11). Middle: correlation coefficient  $C$ . Bottom: amplitude ratio  $R = P_{1,2}/P_1$ . On scales of  $2''$  or equivalently 9 kpc,  $C = 0.4$  and  $R = 0.3$ , which correspond to the top left corner of the  $R - C$  maps in Fig. 3, i.e. mostly isobaric fluctuations. On scales of  $20''$ , about the thickness of the ring in the right panel in Fig. 11, the values of  $R$  and  $C$  both increase to 0.5, corresponding to an increased contribution from adiabatic processes which make up about 30% of the variance of density fluctuations at these smaller scales.

tion from adiabatic processes which make up about 30% of the variance of density fluctuations at these smaller scales.

## 6. ENERGY CONTENT OF THE FLUCTUATIONS

We now relate the total excess energy, associated with fluctuations, to the observed integrated variance  $M^2$ . Consider, for example, the density fluctuations produced by a collection of bubbles of relativistic plasma, occupying a fraction  $f_b \ll 1$  of the cluster volume. We assume that the bubbles are completely devoid from thermal plasma. Therefore, in X-ray observations they correspond to density fluctuations  $\delta\rho/\langle\rho\rangle \sim -1$ . The resulting total variance (to leading order in  $f_b$ ) is

$$M^2 = \left\langle \left( \frac{\delta\rho}{\langle\rho\rangle} \right)^2 \right\rangle \sim f_b. \quad (7)$$

Since the free energy, associated with bubbles is their enthalpy  $E_b = \frac{\gamma}{\gamma-1} P V_b$  (Churazov et al. 2001), we can write  $E_b = \gamma f_b E_{\text{thermal}}$ , where  $V_b$  is the volume occupied by bubbles and  $E_{\text{thermal}} = \frac{1}{\gamma-1} P V$  is the total energy in the volume of the region under consideration,  $V$ . Thus

$$\frac{E_b}{E_{\text{thermal}}} \sim \gamma M^2. \quad (8)$$

Similar expressions can be derived for density fluctuations due to sound waves or gravity waves, they all have

the form  $\frac{E_{\text{fluctuation}}}{E_{\text{thermal}}} \sim \alpha M^2$ , where  $\alpha$  is of order unity (Zhuravleva et al. in prep). Therefore, independently of the nature of fluctuations, we can crudely estimate the total energy associated with fluctuations as  $\approx M^2$ .

To estimate the total variance of density fluctuations,  $M^2$ , we will use the power or amplitude spectra of the 1–3.5 keV images, since these correspond most closely to density fluctuations. In terms of the power this reads

$$M^2 = \int_{k_1}^{k_2} P_{3D}(k) 4\pi k^2 dk \quad (9)$$

where  $P_{3D}(k)$  is the de-projected power spectrum and  $k$  is the spatial wave number. In terms of the 3D amplitude of fluctuations, as plotted in the top panels in Figs. 8 and 10 this equates to

$$M^2 = \int_{k_1}^{k_2} \frac{A_{3D}^2(k)}{k} dk. \quad (10)$$

We integrated the 3D amplitude spectra obtained for the entire  $14' \times 14'$  region in the 1–3.5 keV band, between  $k_1 = 0.005 \text{ arcsec}^{-1}$  and  $k_2 = 0.05 \text{ arcsec}^{-1}$  obtaining a value of  $M^2 \sim 0.05$ . This limited range in spatial scales used for the integration (see Eq. 10) evidently results in a lower limit to the total variance of density fluctuations. We do not expect a large contribution to the variance from larger  $k$  since the amplitude spectrum declines with increasing  $k$ . On the other end,  $k < k_1$ , corresponding to larger scales, could potentially provide a significant contribution to the variance. However, the value of  $k_1$  is not far from  $1/R$  where  $R$  is the size of the region. It is therefore unlikely that our estimates of the total variance at scales  $< R$  are underestimated by a large factor.

For the  $14' \times 14'$  region,  $M^2 \sim 0.05$  as discussed above, implying that in this region the amount of non-thermal energy is  $\sim 5\%$  of the total thermal energy. From here we can estimate that the time  $t_{\text{diss}}$  needed to convert this non-thermal energy into heat in order to balance the cooling losses is  $t_{\text{diss}} = t_{\text{cooling}} \times E_{\text{fluctuation}}/E_{\text{thermal}} \sim 0.05 t_{\text{cooling}}$ . For typical conditions in cool-core clusters, this corresponds to the dynamic timescale, within a factor of a few. This timescale is consistent with the AGN feedback model (Churazov et al. 2000, 2001) when bubbles of relativistic plasma initially capture much of the AGN mechanical power and then transfer energy to the gas on times scales set by the rise of buoyant bubbles. According to this model, the energy goes into turbulence and gravity waves—including the contribution of entrained gas—and dissipates into heat.

A similar analysis can be done for the amplitude spectra of selected regions, as shown in Figs. 9 and 10. In this case we took two approaches. First, we integrate the amplitude spectrum directly, in a range of scales where this spectrum is reliably measured. Then we used this range of  $k$  to fit a powerlaw model to the amplitude spectra and integrated the model over the same range of  $k$  as used above for the entire image i.e.  $k = 0.005 - 0.05 \text{ arcsec}^{-1}$ . The results, with both methods in each region, are summarised in Table 1. The  $M^2$  in the arms region is about four times higher than for the entire image, which has the arms contribution to the power diluted by the less

Region	$k$ range	$M^2_{\text{direct}}$	$k$ range	$M^2_{\text{fit}}$
all	0.005–0.05	0.058	0.005–0.05	0.053
center	0.007–0.1	0.11	0.005–0.05	0.098
arms	0.01–0.1	0.18	0.005–0.05	0.22
shock	0.007–0.04	0.016	0.005–0.05	0.019
outer	0.005–0.02	0.012	0.005–0.05	0.015

TABLE 1

Integrated power of density fluctuations for the regions noted in the left column. Direct integration of the amplitude spectra are quoted in the third column and analytic integration of the powerlaw fit to the spectra are quoted in the fifth column. The frequency ranges used for each integration are quoted in the second and fourth columns.

perturbed part of the image. The shock and the outer regions have much lower amplitudes, with  $M^2$  about an order of magnitude lower than the arms region.

We can estimate the contribution of each section of the image to the total power as follows. The outer region, where the shocks and arms are excluded, is probably representative of the average conditions in the cluster, i.e. similar bubbles and other structures should also exist in the image regions that have been masked out, perhaps at different position along the line of sight than the arms and shocks. Therefore, the contribution to the total  $M^2$  of these mainly isothermal structures is likely similar to the  $M^2 \sim 0.015$  contribution found in the outer region. The shock region is probably representative of the entire ring with inner radius  $1'.3$  and outer radius  $4'.5$  from the centre, not just the section used for our calculations, that masked out the overlying arms and other structures. Therefore, if no other shocks are present, the shock will contribute with about  $0.02 \times 0.3 = 0.006$  to the total  $M^2$  where the factor of 0.3 accounts for the ratio of areas of the shock ring to the entire  $14 \times 14$  image. For the arms region, if these are the only such structures in the total image then their contribution only needs to be scaled down by the ratio of areas so that the contribution of arms to the total  $M^2$  is  $\sim 0.22 \times 1/9 \sim 0.024$ . Finally, the central region, scaled down by the area ratio contributes with  $\sim 0.1 \times 1/15 = 0.006$ , which in total add up approximately to the variance of the entire region, i.e.  $M^2 \sim 0.05$ .

Note that the dissipation timescale discussed above corresponds to an average time over the entire  $14 \times 14'$  region. Isolating the central region, within  $2'$  from the centre, the corresponding  $M^2 \sim 0.1$  so here  $t_{\text{diss}} \sim 0.1 t_{\text{cooling}}$ . Repeating these calculations for radii up to  $4'$  also produces  $t_{\text{diss}} \sim 0.1 t_{\text{cooling}}$ .

## 7. CONCLUSIONS

In this paper, we demonstrate how adiabatic, isobaric and isothermal fluctuations in the ICM have different impacts on cluster images in different X-ray bands. For our chosen energy bands (1–3.5 and 3.5–7.5 keV) adiabatic fluctuations, such as sound waves or weak shocks, produce larger amplitude in the hard band. On the contrary, isobaric fluctuations, characteristic of subsonic gas displacement, produce larger surface brightness fluctuations in the soft band, while the hard band image might show only a small or even a negative response to the same fluctuations. Isothermal fluctuations, such as bubbles and large scale asymmetries, appear equally strong

in both bands. We have exploited this behaviour of the cluster X-ray emission to study the origin of the features in the ICM that produce the observed surface brightness fluctuations. Of course, there are a number of caveats, associated with this analysis. These include the uncertainty in removal of the global cluster profile using a simplistic  $\beta$ -model; the assumption of small-amplitude linear fluctuations, and the assumption that processes of different type are spatially uncorrelated. We nevertheless believe that the analysis captures important observational signatures of different processes responsible for the observed fluctuations and allows us to identify the most prominent ones.

The most prominent features of the M87 X-ray images had been identified as cool arms and quasi-spherical shocks (see figs. 2a, 9a, 11a in Forman et al. 2007). We isolated the regions that contain these structures and calculated power and cross-power spectra, the correlation coefficient  $C$  and the ratio of amplitudes  $R$ . The derived values of  $R$  and  $C$  show an excellent agreement with the predictions of isobaric fluctuations in the arms region and adiabatic fluctuations in the shock region.

The rest of the cluster is not clearly dominated by a single type of fluctuation. We divided the remaining area into a central  $2'$  circle and an outer region. In the centre, the leading type of fluctuation is isobaric, dominating the variance on scales of  $100''$ . At smaller scales of  $20''$ , adiabatic fluctuations appear and account for about 30% of the variance. The dominance of isobaric structures in the central region is further confirmed by the comparison of the soft 1–3.5 keV to the very soft 0.5–1 keV images (see left and centre panels in Fig. 11). The amplitude ratio  $R$  between these bands is about 0.5 which is consistent with a factor of  $\sim 2$  overdensity region in pressure equilibrium with ambient gas at about 1.6 keV, as shown by the predicted amplitude ratios for isobaric fluctuations between these bands in Fig. 12.

For spatial scales of 5–10 kpc, the outer region is dominated by isothermal fluctuations, which include bubbles and deviations from the spherically-symmetric model used to remove the large scale gradient produced by the potential of the cluster. The measured  $R$  and  $C$  values correspond to about 70% of the variance produced by isothermal processes and the remainder is distributed about equally between adiabatic and isobaric processes. Fluctuations on larger scales, of about 30 kpc point to a larger contribution from isobaric fluctuations. Part of these isobaric and apparently adiabatic fluctuations can be unrelated to the central AGN activity, for example as a result of gas sloshing produced by in-falling substructure.

We show that the energy content of the density fluctuations is proportional to their integrated variance, so that by integrating the amplitude spectra of the 1–3.5 keV images, we can estimate the ratio of non-thermal (fluctuations) energy to the thermal energy. Using this argument, we find a non-thermal energy fraction  $E_{\text{fluctuation}}/E_{\text{thermal}} \sim 0.05$  for the entire  $14' \times 14'$  region centered on M87. From this value we estimate the dissipation time of the fluctuations as  $t_{\text{diss}} \sim 0.05 t_{\text{cooling}}$  in order for these fluctuations to balance radiative cooling. The total variance depends on the region of the

image considered, in particular, in the central  $2'$  radius and the central  $4'$  radius regions the integrated variance is  $M^2 \sim 10\%$ , indicating shorter dissipation timescales of  $t_{\text{diss}} \sim 0.1t_{\text{cooling}}$ . These results broadly agree with an AGN feedback model mediated by bubbles of relativistic plasma.

## ACKNOWLEDGMENTS

We are grateful to Dr. A. Schekochihin for many useful discussions. P.A. acknowledges support from Fondecyt grant 1140304. W.F. acknowledges support from the Smithsonian Astrophysical Observatory and NASA-Chandra archive proposal AR1-12007X.

## REFERENCES

- Arévalo, P., Churazov, E., Zhuravleva, I., Hernández-Monteagudo, C., & Revnivtsev, M. 2012, *MNRAS*, 426, 1793
- Birzan, L., Rafferty, D. A., McNamara, B. R., Wise, M. W., & Nulsen, P. E. J. 2004, *ApJ*, 607, 800
- Böhringer, H., Nulsen, P. E. J., Braun, R., & Fabian, A. C. 1995, *MNRAS*, 274, L67
- Churazov, E., Brügggen, M., Kaiser, C. R., Böhringer, H., & Forman, W. 2001, *ApJ*, 554, 261
- Churazov, E., Forman, W., Jones, C., & Böhringer, H. 2000, *A&A*, 356, 788
- Churazov, E., Forman, W., Jones, C., & Böhringer, H. 2003, *ApJ*, 590, 225
- Churazov, E., Forman, W., Vikhlinin, A., Tremaine, S., Gerhard, O., & Jones, C. 2008, *MNRAS*, 388, 1062
- Churazov, E., Sunyaev, R., Forman, W., & Böhringer, H. 2002, *MNRAS*, 332, 729
- Churazov, E., Vikhlinin, A., Zhuravleva, I., Schekochihin, A., Parrish, I., Sunyaev, R., Forman, W., Böhringer, H., & Randall, S. 2012, *MNRAS*, 421, 1123
- David, L. P., Nulsen, P. E. J., McNamara, B. R., Forman, W., Jones, C., Ponman, T., Robertson, B., & Wise, M. 2001, *ApJ*, 557, 546
- Dunn, R. J. H. & Fabian, A. C. 2006, *MNRAS*, 373, 959
- Fabian, A. C., Sanders, J. S., Allen, S. W., Crawford, C. S., Iwasawa, K., Johnstone, R. M., Schmidt, R. W., & Taylor, G. B. 2003, *MNRAS*, 344, L43
- Fabian, A. C., Sanders, J. S., Ettori, S., Taylor, G. B., Allen, S. W., Crawford, C. S., Iwasawa, K., Johnstone, R. M., & Ogle, P. M. 2000, *MNRAS*, 318, L65
- Forman, W., Jones, C., Churazov, E., Markevitch, M., Nulsen, P., Vikhlinin, A., Begelman, M., Böhringer, H., Eilek, J., Heinz, S., Kraft, R., Owen, F., & Pahre, M. 2007, *ApJ*, 665, 1057
- Forman, W., Nulsen, P., Heinz, S., Owen, F., Eilek, J., Vikhlinin, A., Markevitch, M., Kraft, R., Churazov, E., & Jones, C. 2005, *ApJ*, 635, 894
- Harris, D. E., Biretta, J. A., Junor, W., Perlman, E. S., Sparks, W. B., & Wilson, A. S. 2003, *ApJL*, 586, L41
- Jordán, A., Côté, P., Ferrarese, L., Blakeslee, J. P., Mei, S., Merritt, D., Milosavljević, M., Peng, E. W., Tonry, J. L., & West, M. J. 2004, *ApJ*, 613, 279
- Marshall, H. L., Miller, B. P., Davis, D. S., Perlman, E. S., Wise, M., Canizares, C. R., & Harris, D. E. 2002, *ApJ*, 564, 683
- McNamara, B. R., Wise, M., Nulsen, P. E. J., David, L. P., Sarazin, C. L., Bautz, M., Markevitch, M., Vikhlinin, A., Forman, W. R., Jones, C., & Harris, D. E. 2000, *ApJL*, 534, L135
- Million, E. T., Werner, N., Simionescu, A., Allen, S. W., Nulsen, P. E. J., Fabian, A. C., Böhringer, H., & Sanders, J. S. 2010, *MNRAS*, 407, 2046
- Molendi, S. 2002, *ApJ*, 580, 815
- Nulsen, P. E. J., David, L. P., McNamara, B. R., Jones, C., Forman, W. R., & Wise, M. 2002, *ApJ*, 568, 163
- Owen, F. N., Eilek, J. A., & Kassim, N. E. 2000, *ApJ*, 543, 611
- Randall, S. W., Forman, W. R., Giacintucci, S., Nulsen, P. E. J., Sun, M., Jones, C., Churazov, E., David, L. P., Kraft, R., Donahue, M., Blanton, E. L., Simionescu, A., & Werner, N. 2011, *ApJ*, 726, 86
- Reynolds, C. S., McKernan, B., Fabian, A. C., Stone, J. M., & Vignelli, J. C. 2005, *MNRAS*, 357, 242
- Simionescu, A., Werner, N., Forman, W. R., Miller, E. D., Takei, Y., Böhringer, H., Churazov, E., & Nulsen, P. E. J. 2010, *MNRAS*, 405, 91
- Vikhlinin, A., Markevitch, M., Murray, S. S., Jones, C., Forman, W., & Van Speybroeck, L. 2005, *ApJ*, 628, 655
- Werner, N., Zuhone, J. A., Zhuravleva, I., Ichinohe, Y., Simionescu, A., Allen, S. W., Markevitch, M., Fabian, A. C., Keshet, U., Roediger, E., Ruszkowski, M., & Sanders, J. S. 2015, *ArXiv e-prints*
- Young, A. J., Wilson, A. S., & Mundell, C. G. 2002, *ApJ*, 579, 560
- Zhuravleva, I., Churazov, E., Arévalo, P., Schekochihin, A. A., Allen, S. W., Fabian, A. C., Forman, W. R., Sanders, J. S., Simionescu, A., Sunyaev, R., Vikhlinin, A., & Werner, N. 2015, *ArXiv e-prints*
- Zhuravleva, I., Churazov, E., Schekochihin, A. A., Allen, S. W., Arévalo, P., Fabian, A. C., Forman, W. R., Sanders, J. S., Simionescu, A., Sunyaev, R., Vikhlinin, A., & Werner, N. 2014, *Nature*, 515, 85



